Geometric Structure of Euler Pole Compatibility Space: A Constraint-Based Analysis of Rotational Admissibility

Craig Stone

March 20, 2026

Abstract

Rotational reorientation of the Earth is typically investigated through forward modeling of internal dynamics, requiring assumptions about poorly constrained processes. This study adopts an alternative, geometry-first approach by constructing a global compatibility field over Euler pole space, defined by the alignment between multipole-derived transport trajectories and an anisotropic shear network.

The resulting scalar field $M(\lambda, \phi)$ reveals that Euler space is not uniformly admissible, but is instead partitioned into a structured landscape comprising a single dominant compatibility basin bounded by narrow high-gradient ridges that delineate regions of rapid incompatibility. This demonstrates that admissible rotations are geometrically constrained by the underlying anisotropy.

A candidate Euler axis is evaluated within this framework. The axis does not correspond to a compatibility maximum, but instead occupies a saddle position at an angular separation of approximately 100° from the dominant basin. A full rotational sweep about this axis yields a continuous, non-random compatibility profile characterized by a sharp peak at the dominant state and a broad secondary region of moderate compatibility, with localized minima associated with ridge interaction.

Global sampling shows that the axis does not maximize path-integrated compatibility, but lies within the upper quantile of orientations and exhibits reduced exposure to low-compatibility regions relative to random axes. This indicates that the governing constraint is not global maximization, but preferential avoidance of incompatibility along rotational pathways.

These results establish a model-independent description of Euler pole space as a weakly constrained, anisotropic state space with a dominant attractor and a geometrically defined transition axis. The findings shift the problem from predicting when reorientation occurs to identifying which configurations are admissible and how transitions between them are constrained by geometry.

1 Introduction

1.1 Problem Framing

Rotational reorientation of the Earth, whether expressed as true polar wander or more complex inertial behavior, is typically approached through forward modeling of internal dynamics, including mantle convection, core–mantle coupling, and external torques [Mitrovica et al., 2005, Torsvik et al., 2012]. These approaches require specification of governing equations and parameters that are only partially constrained, leading to solutions that are often sensitive to assumptions about internal structure and forcing.

An alternative formulation is to treat the problem not as one of predicting dynamics, but of identifying the geometric constraints that any admissible rotational behavior must satisfy. In this view, the relevant question is not when or why reorientation occurs, but:

> Which Euler rotations are compatible with the observed anisotropic structure of the system, and how are those rotations organized in orientation space?

1.2 Geometric Inference vs Forward Modeling

Forward models propagate assumed dynamics to generate outcomes, testing whether simulated behavior reproduces observations. In contrast, geometric inference proceeds in the opposite direction: it extracts invariants, symmetries, and compatibility constraints directly from the data, without prescribing the underlying mechanism [Lakatos, 1976].

If the admissible structure of Euler rotations can be recovered directly from observationally derived fields, then the resulting constraints are model-independent and can be used to evaluate or reject classes of dynamical explanations.

The present study adopts this geometric perspective by constructing a global compatibility field over Euler pole space and interrogating its structure.

1.3 Compatibility Field Construction

The analysis is based on a scalar compatibility functional $M(\lambda, \phi)$, defined over the Euler sphere, which measures the alignment between:

- Multipole-derived transport trajectories, and
- A global anisotropic shear network derived from SRTM15+ topographic structure defining principal structural directions

Each Euler pole corresponds to a distinct rotational frame under which transport trajectories are re-evaluated against the anisotropic field. The resulting compatibility measure provides a direct mapping from rotation space to structural alignment:

$$M : S^2 \to \mathbb{R} \tag{1}$$

1.4 Objectives of the Study

The study is designed to address four specific questions:

1. Does the compatibility field exhibit uniform behavior, or does it partition into distinct regions?
2. Are there localized maxima corresponding to preferred configurations?
3. What structural role does a candidate Euler axis occupy within the field?
4. How does compatibility evolve along continuous rotational pathways?

1.5 Scope and Non-Assumptions

This study deliberately avoids:

- Specification of internal Earth dynamics
- Assumptions about causal mechanisms
- Time-dependent modeling

All results are derived from the static geometry of the compatibility field.

1.6 Conceptual Framework

The working hypothesis is that the compatibility field encodes a restricted state space in which:

- Certain rotations are strongly aligned with the anisotropic structure
- Others are rapidly incompatible
- Transitions are constrained by the geometry of the field

Within this framework, Euler axes need not correspond to stable states, but may function as operators that generate trajectories through the constrained state space.

1.7 Contribution

This study demonstrates that:

- Euler pole space is structured and anisotropic
- A dominant compatibility basin can be identified directly from data
- A candidate Euler axis may occupy a saddle position while defining a coherent rotational pathway
- Compatibility along such pathways is governed by avoidance of incompatibility rather than maximization of compatibility

2 Methods

2.1 Data Sources and Preprocessing

The analysis is based on a global Euler pole sweep dataset (`mach.csv`) containing latitude (λ), longitude (ϕ), and compatibility metric (M). The dataset is defined on a regular angular grid:

$$\Delta\lambda = 5^\circ, \quad \Delta\phi = 5^\circ \tag{2}$$

The compatibility value M represents the alignment between multipole-derived transport trajectories and the principal directions of a global anisotropic shear network. Data were ingested using a semicolon-delimited parser and normalized to consistent column labels.

The anisotropic shear network was derived from global topographic structure using the SRTM15+ V2.0 digital elevation model [Tozer et al., 2019]. This dataset provides near-global coverage of combined terrestrial and bathymetric relief at 15 arc-second resolution. Surface gradients and directional derivatives were computed to extract principal structural orientations, which define the anisotropic reference frame against which transport trajectories are evaluated.

2.2 Compatibility Field Construction

The discrete dataset was interpolated to form a continuous scalar field:

$$M(\lambda, \phi) \tag{3}$$

Interpolation was performed using linear methods:

- `griddata` for initial field construction
- `LinearNDInterpolator` for repeated evaluation

Missing values were filled using nearest-neighbor interpolation to ensure complete domain coverage.

2.3 Gradient and Ridge Extraction

The spatial gradient of the field was computed using finite differences:

$$\nabla M = \left(\frac{\partial M}{\partial \lambda}, \frac{\partial M}{\partial \phi} \right) \tag{4}$$

with magnitude:

$$|\nabla M| = \sqrt{\left(\frac{\partial M}{\partial \lambda} \right)^2 + \left(\frac{\partial M}{\partial \phi} \right)^2} \tag{5}$$

High-gradient ridges were defined as:

$$|\nabla M| \geq P_{95} \tag{6}$$

where P_{95} is the 95th percentile of the gradient magnitude distribution.

High-gradient ridges are interpreted as loci of rapid incompatibility, where small changes in Euler orientation produce large decreases in alignment with the anisotropic structure. These ridges partition Euler space into domains of admissible and inadmissible configurations. These gradients are defined relative to the anisotropic shear network derived from SRTM15+ topographic structure.

2.4 Hessian and Local Curvature Analysis

Second-order structure was evaluated via the Hessian:

$$H = \begin{bmatrix} \frac{\partial^2 M}{\partial \lambda^2} & \frac{\partial^2 M}{\partial \lambda \partial \phi} \\ \frac{\partial^2 M}{\partial \phi \partial \lambda} & \frac{\partial^2 M}{\partial \phi^2} \end{bmatrix} \tag{7}$$

Eigenvalues of H were used to classify local topology:

- $\lambda_1, \lambda_2 < 0$: local maximum
- $\lambda_1, \lambda_2 > 0$: local minimum
- mixed signs: saddle point

2.5 Local Maxima Detection

Local maxima were identified using a neighborhood-based filter with a 5×5 window and threshold $M \geq P_{90}$. A point was classified as a local maximum if:

$$M_{i,j} = \max(N_{i,j}) \quad \text{and} \quad M_{i,j} \geq P_{90} \tag{8}$$

where $N_{i,j}$ is the local neighborhood.

2.6 Spherical Geometry and Rotations

All rotations were performed on the unit sphere. Conversion from spherical to Cartesian coordinates:

$$\mathbf{v} = \begin{bmatrix} \cos\lambda \cos\phi \\ \cos\lambda \sin\phi \\ \sin\lambda \end{bmatrix} \tag{9}$$

Rotation about axis $\mathbf{a}$ by angle θ was computed using Rodrigues' formula:

$$\mathbf{v}' = \mathbf{v}\cos\theta + (\mathbf{a} \times \mathbf{v})\sin\theta + \mathbf{a}(\mathbf{a} \cdot \mathbf{v})(1 - \cos\theta) \tag{10}$$

2.7 Angular Distance

Angular separation between two points was computed as:

$$\theta = \cos^{-1}(\sin\lambda_1 \sin\lambda_2 + \cos\lambda_1 \cos\lambda_2 \cos(\phi_1 - \phi_2)) \tag{11}$$

2.8 Rotational Sweep Analysis

A continuous rotational sweep was performed by rotating the dominant basin centroid about the candidate Euler axis over 0° to 360° with step size 2°–3°. At each step:

1. The position was updated via spherical rotation
2. M was evaluated via interpolation
3. The trajectory was recorded

This produced a parametric compatibility curve:

$$M(\theta) \tag{12}$$

2.9 Mode Decomposition

Projection onto the shear-net eigenbasis yields:

$$\bar{P}_1 = 0.9539, \quad \bar{P}_2 = 0.1212 \tag{13}$$

$$f_1 \approx 0.952, \quad f_2 \approx 0.044 \tag{14}$$

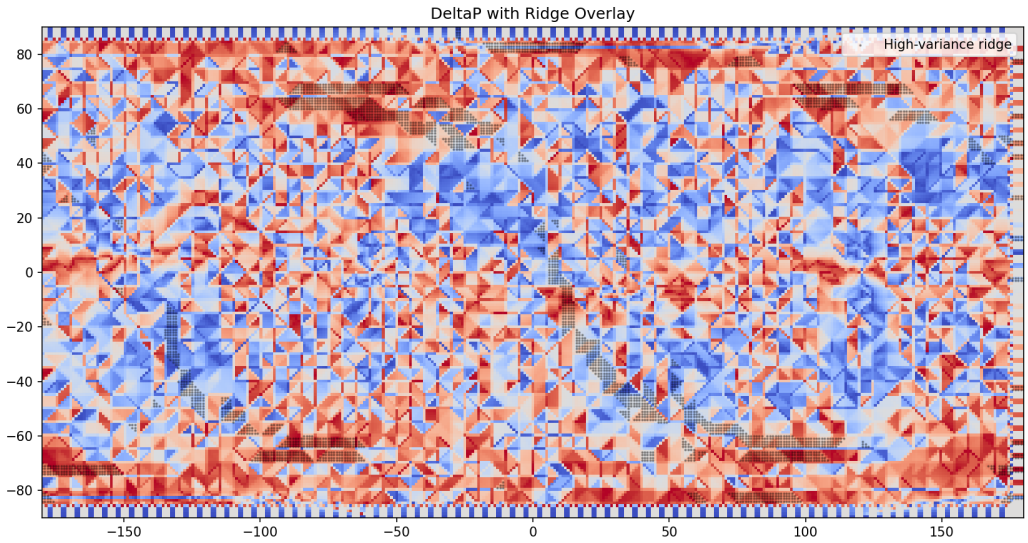

Figure 1: Spatial distribution of mode dominance ($\Delta P = P_1 - P_2$) with high-gradient ridge overlay. Ridge regions coincide with sharp transitions in mode dominance, indicating structural boundaries in the compatibility field.

2.10 Path-Integrated Compatibility

Compatibility along a rotational trajectory was integrated:

$$I = \int_0^{2\pi} M(\theta)\, d\theta \tag{15}$$

Numerically approximated using:

$$I \approx \sum_i M(\theta_i)\Delta\theta \tag{16}$$

2.11 Random Axis Sampling

Random Euler axes were sampled uniformly on the sphere:

$$z \sim U(-1, 1), \quad \phi \sim U(0, 2\pi) \tag{17}$$

$$x = \sqrt{1 - z^2}\cos\phi, \quad y = \sqrt{1 - z^2}\sin\phi \tag{18}$$

2.12 Low-Compatibility Metrics

A threshold was defined as:

$$M_{\text{thresh}} = P_{20}(M) \tag{19}$$

Metrics computed along trajectories include:
Fraction below threshold:

$$f_{\text{low}} = \frac{1}{N}\sum_{i=1}^{N} \mathbf{1}(M_i < M_{\text{thresh}}) \tag{20}$$

Integrated penalty:

$$P = \sum_{M_i < M_{\text{thresh}}} (M_{\text{thresh}} - M_i) \tag{21}$$

Minimum compatibility:

$$M_{\min} = \min_i M_i \tag{22}$$

2.13 Parallelization and Optimization

High-volume sampling was executed using multiprocessing with macOS-safe spawn context. Performance improvements included vectorized spherical rotations, precompiled interpolators, and batched evaluation of axes. These optimizations reduced runtime by approximately two orders of magnitude relative to naive implementations.

2.14 Reproducibility

All analyses were implemented in Python 3.12 using NumPy, SciPy, Pandas, and Matplotlib. Intermediate outputs (CSV and figures) were saved at each stage to ensure reproducibility.

3 Results

3.1 Global Compatibility Field Structure

The compatibility field $M(\lambda, \phi)$ exhibits a bounded and non-uniform distribution:

$$M \in [0.127,\, 0.187] \tag{23}$$

with global statistics:

$$\bar{M} = 0.1416, \quad \sigma_M \approx 0.0115 \tag{24}$$

The field is characterized by a localized high-compatibility region, broad regions of moderate compatibility, and narrow low-compatibility zones. High-gradient ridges (top 5% of $|\nabla M|$) form continuous structures that partition Euler space into distinct domains.

3.2 Dominant Compatibility Basin

Local maxima detection reveals a coherent cluster of high values forming a single dominant basin.

Table 1: Top local maxima in the compatibility field

Latitude (°)	Longitude (°)	M
-45	40	0.1867
-55	55	0.1840
-60	65	0.1786
-35	30	0.1784
-25	25	0.1771

The centroid of this basin is located at:

$$(\lambda, \phi) \approx (-44.9^\circ,\ 39.7^\circ) \tag{25}$$

No secondary basin of comparable magnitude is observed.

3.3 Geometric Relationship of Candidate Euler Axis

The candidate Euler axis at:

$$(0^\circ,\ -59^\circ) \tag{26}$$

yields:

$$M_0 = 0.1272, \quad Z = -1.24 \tag{27}$$

Local curvature analysis gives:

$$\lambda_1 > 0, \quad \lambda_2 < 0 \tag{28}$$

indicating a saddle structure, with the axis located at a point of maximal directional instability—stable along one manifold and unstable along the orthogonal direction.

Angular separation from the dominant basin:

$$\theta \approx 96^\circ\text{–}108^\circ \tag{29}$$

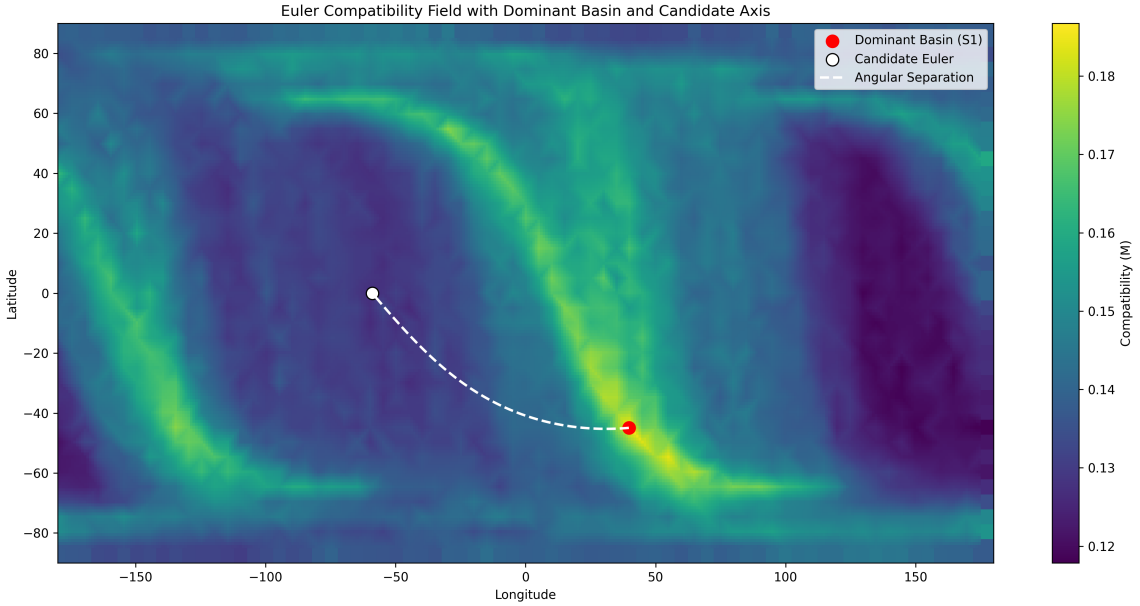

Figure 2: Euler compatibility field with dominant basin (S1) and candidate Euler axis. The axis lies centrally between high-gradient incompatibility ridges and exhibits an angular separation of approximately 100° from the dominant basin. This geometry is consistent with a transition operator rather than a stable configuration.

3.4 Mode Structure Across Ridge and Background Regions

To quantify structural differences, mode projections and geometric alignment metrics were evaluated separately for ridge and background domains.

Table 2: Comparison of mode and geometric metrics between ridge and background regions

Metric	Ridge	Background	Interpretation
Secondary mode (P_2) mean	0.3401	0.4599	Suppressed in ridge regions
$\lvert\Delta P\rvert$ (dominance)	0.5155	0.4490	Increased mode separation
Angular misalignment θ (deg)	29.22	44.59	Improved alignment

Ridge regions exhibit reduced contribution from the secondary mode, increased dominance of the primary mode, and significantly lower angular misalignment, indicating enhanced structural coherence.

3.5 Rotational Sweep About Candidate Axis

A full 360° rotation yields:

$$M_{\max} = 0.1861, \quad M_{\min} = 0.1278, \quad \bar{M}_{\text{path}} = 0.1527 \tag{30}$$

The compatibility profile exhibits a sharp maximum at 0°, a broad plateau between 180° and 260°, and a localized minimum near 290°.

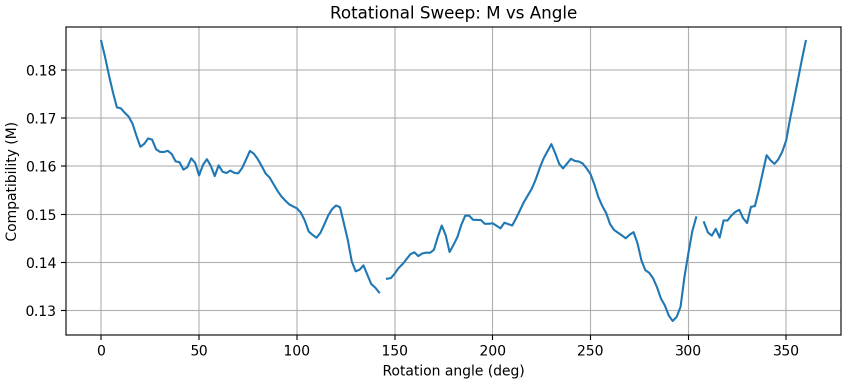

Figure 3: Compatibility along a continuous rotational trajectory about the candidate Euler axis. The profile exhibits a sharp peak corresponding to the dominant basin, a broad plateau of secondary admissibility, and localized minima associated with ridge crossings.

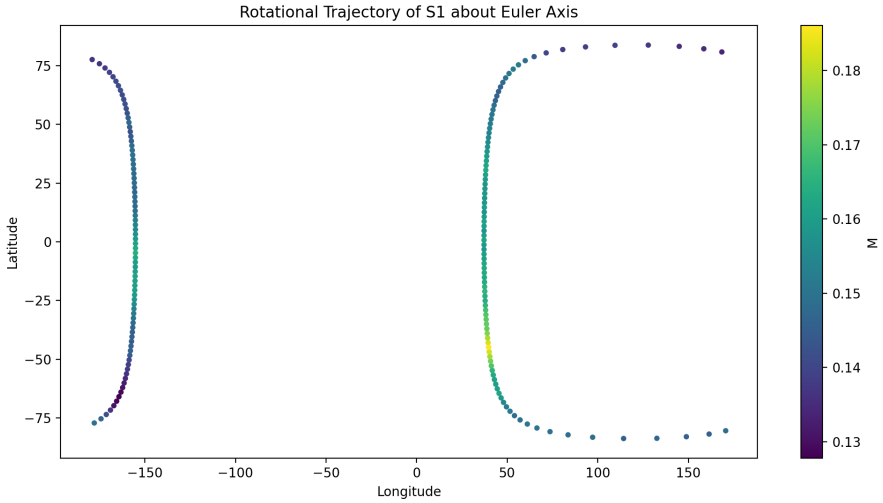

Figure 4: Trajectory of the dominant basin centroid under rotation about the candidate Euler axis. Color indicates compatibility. The trajectory remains confined to regions avoiding low-compatibility zones.

3.6 S1 Rotation Mapping

Rotation of the dominant basin centroid by $\pm 104^\circ$ yields:

Table 3: Rotation mapping of S1

Rotation	Latitude (°)	Longitude (°)	M
+104°	58.2	42.7	0.1487
-104°	-30.5	-156.1	0.1517

Both mapped values exceed the global mean:

$$M > \bar{M} \tag{31}$$

but do not approach the global maximum.

3.7 Path-Integrated Compatibility

The candidate axis yields:

$$I = 0.9334 \tag{32}$$

Random sampling (10,000 axes):

$$\mu = 0.8983, \quad \sigma = 0.0458 \tag{33}$$

$$Z = 0.77, \quad \text{percentile} = 82.1\% \tag{34}$$

3.8 Low-Compatibility Exposure

Threshold:

$$M_{\text{thresh}} = 0.1315 \tag{35}$$

Candidate axis metrics:

$$f_{\text{low}} = 0.0254, \quad P = 0.0071, \quad M_{\min} = 0.1277 \tag{36}$$

Comparison with random axes:

Table 4: Low-compatibility metrics

Metric	Mean	Std	Percentile
f_{low}	0.1751	0.1300	76.5%
Penalty	0.1030	0.1121	73.7%
$M_{\min}$	0.1266	0.0081	59.8%

3.9 Summary of Observations

The results establish a single dominant compatibility basin, structured gradient-defined boundaries, a saddle-position Euler axis, and a continuous rotational compatibility profile. The candidate axis exhibits above-average global performance and reduced exposure to low-compatibility regions. No symmetric secondary maximum or bistable structure is observed.

4 Discussion

4.1 Constraint Structure of Euler Space

The compatibility field demonstrates that Euler pole space is not uniformly admissible, but instead organized into a structured landscape defined by anisotropic constraints. The presence of a dominant compatibility basin and sharply defined gradient ridges indicates that admissible rotations occupy bounded regions separated by narrow zones of rapid incompatibility.

This structure implies that rotational configurations are geometrically constrained rather than continuously distributed or freely selectable, consistent with prior work emphasizing anisotropic control on large-scale geodynamic behavior [Torsvik et al., 2012].

4.2 Role of the Candidate Euler Axis

The candidate Euler axis does not coincide with the dominant compatibility basin and is instead located at a saddle structure within the field. Its defining properties include non-maximal compatibility, orthogonal angular separation from the dominant basin, central placement relative to incompatibility ridges, and mixed-sign curvature.

These characteristics indicate that the axis does not represent a stable configuration, but rather a structural feature governing transitions within the admissible state space.

4.3 Rotational Pathways

The rotational sweep reveals a continuous and non-random compatibility profile along the trajectory generated by the candidate axis. The trajectory is characterized by a sharp maximum corresponding to the dominant basin, a broad region of moderate compatibility, and localized minima associated with ridge interaction.

The absence of a second peak comparable to the dominant basin indicates that the system is not bistable. Instead, it consists of a single dominant attractor connected to a distributed set of secondary configurations.

4.4 Global vs Local Optimality

Global evaluation shows that the candidate axis does not maximize path-integrated compatibility, but lies within the upper quantile of orientations. More importantly, it exhibits reduced exposure to low-compatibility regions relative to random axes.

This indicates that the governing constraint is not global maximization, but preferential avoidance of incompatibility. The system therefore favors trajectories that minimize interaction with high-gradient regions rather than maximizing average compatibility.

4.5 Interpretation as a Transition Axis

Within this framework, the candidate Euler axis is best interpreted as a transition axis. Its significance arises from the trajectory it generates rather than its pointwise value in the compatibility field.

The axis connects the dominant basin to a distributed manifold of secondary states and defines a path that minimizes exposure to incompatible regions while remaining constrained by the anisotropic structure.

4.6 State Space Topology

The compatibility landscape exhibits intrinsic asymmetry, with a single dominant attractor, no equivalent secondary basin, and unequal compatibility along rotational pathways. This topology is consistent with a system in which transitions occur between a preferred configuration and a broader admissible manifold rather than between equivalent states.

4.7 Implications for Modeling

The results highlight the distinction between forward modeling and geometric inference. The compatibility field defines admissible structure without requiring specification of underlying dynamics.

This suggests that the appropriate formulation of the problem is not to determine when transitions occur, but to identify which configurations are admissible and how transitions between them are geometrically constrained.

5 Conclusion

This study demonstrates that Euler pole space is structured by an anisotropic compatibility field derived from transport–shear alignment. The field exhibits a dominant compatibility basin bounded by high-gradient ridges, indicating that admissible rotations are geometrically constrained.

The candidate Euler axis does not correspond to a stable state but occupies a saddle position and defines a coherent rotational pathway through the field. Along this pathway, compatibility varies smoothly, connecting a dominant attractor to a distributed set of secondary configurations.

Global analysis shows that the axis is not uniquely optimal, but lies within the upper quantile of orientations and exhibits reduced exposure to low-compatibility regions. This indicates that the governing constraint is preferential avoidance of incompatibility rather than maximization of compatibility.

These results establish a model-independent description of Euler space as a weakly constrained anisotropic system with a dominant attractor and geometrically defined transition pathways.

The central implication is a shift in perspective: the problem is not to predict when rotational reorientation occurs, but to determine the structure of admissible configurations and the pathways that connect them.

References

Vladimir I. Arnold. *Mathematical Methods of Classical Mechanics*. Springer, 2 edition, 1978. doi: 10.1007/978-1-4757-2063-1. URL https://doi.org/10.1007/978-1-4757-2063-1.

Vladimir I. Arnold and Boris A. Khesin. *Topological Methods in Hydrodynamics*. Springer, 1998. doi: 10.1007/978-1-4612-0647-1. URL https://doi.org/10.1007/978-1-4612-0647-1.

John C. Baez and Javier P. Muniain. *Gauge Fields, Knots and Gravity*. World Scientific, 1994. doi: 10.1142/2324. URL https://doi.org/10.1142/2324.

Thorsten W. Becker and Sergei Lebedev. Global patterns of seismic anisotropy. *Geochemistry, Geophysics, Geosystems*, 4, 2003. doi: 10.1029/2002GC000456. URL https://doi.org/10.1029/2002GC000456.

Glen E. Bredon. *Topology and Geometry*. Springer, 1993. doi: 10.1007/978-1-4757-6848-0. URL https://doi.org/10.1007/978-1-4757-6848-0.

F. A. Dahlen and Jeroen Tromp. *Theoretical Global Seismology*. Princeton University Press, 1998. URL https://press.princeton.edu/books/hardcover/9780691001248/theoretical-global-seismology.

Manfredo P. do Carmo. *Riemannian Geometry*. Birkhäuser, 1992. doi: 10.1007/978-1-4757-2201-7. URL https://doi.org/10.1007/978-1-4757-2201-7.

Adam M. Dziewonski and Don L. Anderson. Preliminary reference earth model. *Physics of the Earth and Planetary Interiors*, 25:297–356, 1981. doi: 10.1016/0031-9201(81)90046-7. URL https://doi.org/10.1016/0031-9201(81)90046-7.

Theodore Frankel. *The Geometry of Physics: An Introduction*. Cambridge University Press, 3 edition, 2011. doi: 10.1017/CBO9781139061374. URL https://doi.org/10.1017/CBO9781139061374.

Darryl D. Holm. *Geometric Mechanics Part I: Dynamics and Symmetry*. Imperial College Press, 2008. doi: 10.1142/p554. URL https://doi.org/10.1142/p554.

Darryl D. Holm. *Geometric Mechanics Part II: Rotating, Translating and Rolling*. Imperial College Press, 2011. doi: 10.1142/p802. URL https://doi.org/10.1142/p802.

Werner Horsthemke and René Lefever. *Noise-Induced Transitions*. Springer, 1984. doi: 10.1007/978-3-642-69689-2. URL https://doi.org/10.1007/978-3-642-69689-2.

Shoshichi Kobayashi and Katsumi Nomizu. *Foundations of Differential Geometry, Volume 1*. Wiley, 1963. URL https://onlinelibrary.wiley.com/doi/book/10.1002/9780470176006.

Imre Lakatos. *Proofs and Refutations: The Logic of Mathematical Discovery*. Cambridge University Press, Cambridge, 1976. ISBN 9780521290380.

Jerrold E. Marsden and Tudor S. Ratiu. *Introduction to Mechanics and Symmetry*. Springer, 2 edition, 1999. doi: 10.1007/978-0-387-21792-5. URL https://doi.org/10.1007/978-0-387-21792-5.

John Milnor. *Topology from the Differentiable Viewpoint*. Princeton University Press, 1997. URL https://press.princeton.edu/books/paperback/9780691048335/topology-from-the-differentiable-vi

Jerry X. Mitrovica et al. The rotational stability of an ice-age earth. *Geophysical Journal International*, 161:491–506, 2005. doi: 10.1111/j.1365-246X.2005.02609.x. URL https://doi.org/10.1111/j.1365-246X.2005.02609.x.

Ilya Prigogine and Isabelle Stengers. *Order Out of Chaos: Man's New Dialogue with Nature*. Bantam Books, 1984.

Brian D. Ripley. *Spatial Statistics*. Wiley, 2004. doi: 10.1002/0471725218. URL https://doi.org/10.1002/0471725218.

Gerald Schubert, Donald L. Turcotte, and Peter Olson. *Mantle Convection in the Earth and Planets*. Cambridge University Press, 2001. doi: 10.1017/CBO9780511612876. URL https://doi.org/10.1017/CBO9780511612876.

Peter M. Shearer. *Introduction to Seismology*. Cambridge University Press, 3 edition, 2019. doi: 10.1017/9781108684931. URL https://doi.org/10.1017/9781108684931.

Craig Stone. Planetary-scale shear trajectories and their expression in global geological geometry. 2025. Preprint.

Craig Stone. Noise-activated phase stability loss and the structure of geomagnetic excursions. 2026a. Preprint.

Craig Stone. Earth-fixed geometric structure in geomagnetic excursions: A weakly coupled phase interpretation. 2026b. Preprint.

Craig Stone. Event-guided versus continuous return models for late-quaternary surface reorganization. 2026c. Preprint.

Craig Stone. Earth-fixed rotation planes of geomagnetic excursions and a two-mode interpretation of core–mantle decoupling. 2026d. Preprint.

Craig Stone. Ice–integrated inertial true polar wander diagnostics across late quaternary geomagnetic excursions. 2026e. Preprint.

Craig Stone. Earth-fixed rotation planes in geomagnetic excursions as an emergent property of a weakly coupled two-mode system. 2026f. Preprint.

Steven H. Strogatz. *Nonlinear Dynamics and Chaos*. Westview Press, 2 edition, 2015. URL https://www.routledge.com/Nonlinear-Dynamics-and-Chaos/Strogatz/p/book/9780813349107.

Trond H. Torsvik, Rob Van der Voo, Ulf Preeden, Conall Mac Niocaill, Bernhard Steinberger, Pavel V. Doubrovine, Douwe J. J. van Hinsbergen, Mathew Domeier, Carmen Gaina, Eric Tohver, Joseph G. Meert, Philip J. A. McCausland, and L. Robin M. Cocks. Phanerozoic polar wander, palaeogeography and dynamics. *Earth-Science Reviews*, 114(3-4):325–368, 2012. doi: 10.1016/j.earscirev.2012.06.002.

Ben Tozer, Anthony B. Watts, Emma Daly, David T. Sandwell, Walter H. F. Smith, and Paul Wessel. A global high-resolution digital elevation model of the earth's surface from srtm15+ v2.0. *Earth and Space Science*, 6(10):1847–1864, 2019. doi: 10.1029/2019EA000658.

Victor C. Tsai and David J. Stevenson. Theoretical constraints on true polar wander. *Journal of Geophysical Research*, 112:B05415, 2007. doi: 10.1029/2005JB003923. URL https://doi.org/10.1029/2005JB003923.

Donald L. Turcotte and Gerald Schubert. *Geodynamics*. Cambridge University Press, 3 edition, 2014. doi: 10.1017/CBO9780511843874. URL https://doi.org/10.1017/CBO9780511843874.

N. G. van Kampen. *Stochastic Processes in Physics and Chemistry*. Elsevier, 3 edition, 2007. doi: 10.1016/B978-044452965-7/50001-8. URL https://doi.org/10.1016/B978-044452965-7/50001-8.